Electronic Supplementary Material (ESI) for Chemical Science.

Supporting Information

Hydrous Ruthenium Oxide Triggers Template-free and Spontaneous Growth of Metal Nanostructures

Faheem Muhammad[a,#], Xiwen Chen[a,#], Jiayi Tang[a,#], Yuan Cheng[a], Yuyang Li[b], Chenxin Zhu[a], Yihong Zhang[a], Leiying Miao[b], Yu Deng[a], Hui Wei[a,c]*

[a]*College of Engineering and Applied Sciences, Nanjing National Laboratory of Microstructures, Jiangsu Key Laboratory of Artificial Functional Materials, Nanjing University, Nanjing, Jiangsu 210023, China.*
[b]*Department of Cariology and Endodontics, Nanjing Stomatological Hospital, Medical School of Nanjing University, Nanjing, 210008, China.*
[c]*State Key Laboratory of Analytical Chemistry for Life Science, School of Chemistry and Chemical Engineering, Chemistry and Biomedicine Innovation Center (ChemBIC), Nanjing University, Nanjing, Jiangsu 210023, China.*

# These authors contributed equally to this work.

Chemicals and reagents. Ruthenium chloride hydrate ($RuCl_3 \cdot xH_2O$), potassium tetrachloroplatinate (II) (K_2PtCl_4), silver nitrate ($AgNO_3$), chloroauric acid ($HAuCl_4 \cdot 4H_2O$), sodium hydroxide (NaOH), ammonium hydroxide (25% NH_4OH), Citric acid monohydrate ($C_6H_8O_7 \bullet H_2O$), acetone and commercial RuO_2 were purchased from Aladdin Chemical Co. Ltd. (Shanghai, China). Hoechst 33342 staining solution, dimethyl sulfoxide (DMSO), and Cell Counting Kit-8 (CCK-8) were acquired from Beyotime, China. Colitis grade dextran sulfate sodium (DSS, 36~50 kDa) was purchased from MP Biomedicals, USA. 2,4,6-Trinitrobenzenesulfonic acid (5% (w/v) in H_2O) was purchased from Innochem, China. 2',7'-Dichlorodihydrofluorescein diacetate (DCFH-DA) was obtained from MedChemExpress, USA. All other reagents and chemicals were purchased from commercial sources and used as received. Deionized water (18.2 MΩ·cm, Millipore) and absolute ethanol were used throughout the experiments.

Material characterizations. The structural parameters of the materials were investigated using a transmission electron microscope (TEM, FEI TECNAI G2 F20 200 kV, and JOEL, JEM-2800). High-angle annular dark-field scanning transmission electron microscopy (HAADF-STEM) imaging and electron energy-loss spectroscopic (EELS) analysis were carried out on an aberration-corrected STEM Titan Cubed G2 300 system. Powder XRD patterns were recorded using a diffractometer (Bruker-AXS, Germany) with a Cu Kα radiation. The elemental compositions were determined by an inductively coupled plasma optical emission spectrometer (CP-OES, iCAP 7200, Thermo, USA)). X-ray photoelectron spectroscopic (XPS) investigations were performed by a Thermo Scientific K-Alpha spectrometer (Al Kα (1486 eV) using a hemispherical energy analyzer; the binding energy was calibrated by C1*s* at 284.8 eV. UV–vis absorption spectra were obtained using a UV–vis spectrophotometer with a 1 cm quartz cell (Shimadzu Co., Japan) and with a microplate reader (SpectraMax M2e, Molecular Device, USA). Zeta potentials were measured at 25 °C using a Malvern Zetasizer Nano ZS90. For catalase-like activity testing, the generated oxygen (milligram per liter) was monitored using a dissolved oxygen meter (SevenExcellence Multiparameter, Mettler Toledo Co. Ltd.). Raman characterization was performed on an HY LabRAM Evolution Raman Microscope with a 633 nm laser source to analyze the Raman signals of the RuO_2 samples. Thermogravimetric analysis was carried out using a Pyris DSC/0.2 uW (PerkinElmer, USA) instrument. Ultraviolet photoelectron spectroscopy (UPS) was performed using a Thermo Scientific Nexsa G2 X-ray photoelectron spectrometer (XPS) system (USA). A Thermo Scientific Nicolet iS 5 FTIR Spectrometer (USA) was used for FTIR analysis.

Synthesis of ultrasmall hydrous RuO_2 NPs. Citric acid monohydrate (100 mg, 0.47 mmol) was dissolved in 200 mL of water at room temperature, followed by the introduction of ruthenium chloride hydrate (100 mg) under stirring. After the complete dissolution of both precursors, the pH of the solution was increased to 10 with the dropwise addition of NaOH solution. The temperature of the resulting forest green-colored solution was subsequently elevated to 80 °C. Following 60 min of stirring at 80 °C, acetone (200-300 mL) was added to facilitate the flocculation process; the product was then collected by centrifugation (10000 rpm, 10 min) and washed twice with deionized water to remove any unreacted salts. A portion of the freshly prepared wet RuO_2 product was dispersed in water under sonication, whereas the remaining product was dried at 60 °C overnight for further characterization.

Synthesis of RuO_2@Ag nanostructures. Unlike conventional methods, we exploited the redox-active nature of H-RuO_2 NPs to grow Ag NPs. Ten milligrams of an aqueous solution of as-synthesized H-RuO_2 NPs (200 μg/mL) were placed in a beaker containing a stirring bar, and then 1 mL of $AgNO_3$ (10 mg/mL) was added while stirring at room temperature for 24 h. The collected product was analyzed by TEM to track the growth of Ag NPs at different points in time. Synthesis was also performed under alkaline conditions (pH 9). NH_4OH was first added to adjust the pH of the aqueous solution of H-RuO_2 NPs,

followed by the addition of $AgNO_3$. Continuous stirring of the solution for 3 h resulted in the formation of the Ag-studded RuO_2 darkish product, suggesting the successful synthesis of Ag NPs. The product was collected via centrifugation and washed with deionized water to remove unreacted precursors.

Synthesis of RuO_2@Au nanostructures. An aqueous solution (10 mL) of the as-synthesized H-RuO_2 NPs (200 µg/mL) was first introduced into three 20 mL vials with stirring bars. To produce gold with different sizes and nanostructures, the pH of the solutions was varied; the pH of one of the vials remained undisturbed, whereas the pH of the other two vials was changed to 5.0 and 9.0 by adding NaOH solution. Then, 1 mL of $HAuCl_4 \cdot 4H_2O$ (2 mg/mL) was added to each vial while stirring at room temperature. Even though the color of the solutions changed within minutes upon adding the $HAuCl_4$ solution. The reaction was continued for 24 h to track the growth of the self-assembled Au nanostructure at pH 9.0. The different colored products generated at varied pH implied the successful synthesis of Au nanostructures with different sizes/structures. The product was collected via centrifugation and washed with deionized water.

Synthesis of RuO_2@Pt nanostructures. Similarly, an aqueous solution (10 mL) of the as-synthesized H-RuO_2 NPs (200 µg/mL) was first added into 20 mL vials with a stirring bar, followed by the addition of 1 mL of K_2PtCl_4 aqueous solution (2 mg/mL) under stirring at room temperature. After stirring for 24 h, the collected product was analyzed by TEM at different time points. In another attempt, we increased the temperature of the reaction medium to 80 °C and stirred the solution for 30 min until a significant change in the color of the solution was observed. The product was finally collected via centrifugation and washed with deionized water.

Surface modification of commercial RuO_2 NPs. Commercial RuO_2 (100 mg) was dispersed into 20 mL of deionized water under intense sonication, followed by the addition of 10 mg sodium citrate. The sample was stirred for 1 h, centrifuged, and washed thrice with water and ethanol.

Synthesis of Pt nanoparticles. In a typical procedure, PVP K30 (266 mg) was dissolved in 90 mL of methanol under magnetic stirring, followed by the addition of 10 mL of 50 mM H_2PtCl_6. The solution was then refluxed for 3 h under vigorous stirring. Afterward, the solution was subjected to rotary evaporation to evaporate the methanol. Pt NPs were precipitated by acetone and then redispersed in water for further use.

Synthesis of Fe_3O_4 nanoparticles. Iron trichloride hexahydrate (700 mg) was dissolved in 20 mL of ethylene glycol, followed by adding 280 mg trisodium citrate under vigorous stirring. After the complete dissolution of both salts, 1.20 g anhydrous sodium acetate was added while stirring the solution. The obtained yellow solution was sealed in an autoclave. The solution was heated in an oven at 200 °C for 10 h. The product was recovered with magnetic separation and then washed multiple times with water and ethanol.

SOD-like activity measurements. The SOD-like activity of different RuO_2 and H-RuO_2@metal nanostructures was evaluated using a SOD assay kit (Dojindo, Japan).[1] In principle, the xanthine oxidase (XO) catalyzes the reaction between water-soluble tetrazolium WST-1 and $O_2^{\cdot-}$ to generate a formazan dye. The SOD-like nanozyme inhibits the reaction, thus enabling to colorimetrically detect the activity. First, 20 µL of each material with a specific concentration was mixed with 200 µL of working solution in a microplate well. Next, the enzyme working solution (20 µL) was introduced, followed by a 20 min incubation at 37 °C. The absorbance at 450 nm was measured using a multiple plate reader (Tecan Infinite 200 Pro). The quenching rate of the superoxide radical was calculated by measuring the inhibition in color development. The analysis was performed in replicates (n = 3).

CAT-like activity measurements. The CAT-like activity of different RuO_2 and H-RuO_2@metal

nanostructures was measured by observing the amount of dissolved oxygen generated with an oxygen meter. Briefly, each material and H_2O_2 were successively added to 6 mL of water. The concentration of RuO_2-based materials was set to 20 μg/mL, and the final concentration of H_2O_2 was maintained at 5 mM. The amount of catalase-like nanozyme-mediated generation of oxygen (milligram per liter) was monitored for up to 10 min.

Catalytic kinetics of catalase-like nanostructures. The catalytic kinetics of catalase-like nanostructures were evaluated using an oxygen electrode. Typically, H-RuO_2 and H-RuO_2@metal nanozymes were added to 2.5 mM, 5 mM, 10 mM, 20 mM, 40 mM, and 80 mM H_2O_2 solutions, and the production of oxygen was monitored by an oxygen electrode. The final concentration of H-RuO_2 and H-RuO_2@metal nanozyme was 1 μg/mL. The concentration of dissolved oxygen was recorded every 5 sec within 1 min. Three repeated measurements were conducted under different concentrations of H_2O_2. Six initial velocities (V_0) were calculated using linear fitting. Afterward, the plot of the six V_0 versus the corresponding [H_2O_2] was fitted using the Michaelis−Menten equation.

Catalase-like activity at different pH values. Typically, 1 μg/mL H-RuO_2@metal nanozymes were added to a 5 mM H_2O_2 solution, and the production of oxygen was monitored by an oxygen electrode. The concentration of dissolved oxygen was recorded every 30 sec within 5 min. The curves of dissolved oxygen versus time were plotted.

Peroxidase-mimicking activity at different pH values. The optimized pH for peroxidase-mimicking activities of H-RuO_2 and H-RuO_2@metal was evaluated by comparing the initial velocity (V_0) of the catalysis of 3,3',5,5'-tetramethylbenzidine (TMB) in the presence of H_2O_2. Typically, 0.02 mM TMB, 1 μg/mL nanozyme materials, and 5 mM H_2O_2 were added in sequence to a cuvette with a final solution of 3 mL. After the addition of H_2O_2, the reactants were quickly mixed with a pipette, and the absorbance under 652 nm was monitored by a spectrophotometer. The initial velocity was calculated based on the Beer−Lambert law. The curve of V_0 versus pH was plotted. Similarly, the peroxidase-mimicking activity of Pt NPs and Fe_3O_4 NPs at different pH values was evaluated following the same protocol described above.

Cell culture and cytotoxicity of RuO_2@metal nanozymes. RAW 264.7 cells were obtained from the cell bank of the Chinese Academy of Sciences (Shanghai, China). Cells were cultured in high glucose-DMEM (Bio-Channel, China) containing 10% (v/v) FBS and 1% penicillin/streptomycin (Cytiva, USA) in a humidified 5% CO_2 atmosphere at 37 °C. To evaluate the cell viability, Raw 264.7 cells were seeded into 96-well plates at a density of 5×10^3 cells per well. The medium was refreshed after overnight incubation, followed by the addition of various H-RuO_2-based nanozymes with different concentrations (0–100 μg/mL). Following incubation for another 24 h, the cells were washed with PBS three times. Cell viability was determined by a CCK (Cell Counting Kit)-8 assay (n = 3), according to the manufacturer's instructions using a microplate reader (Tecan Infinite 200 Pro).

Viability = $(O_t\text{-}O_b)/(O_c\text{-}O_b)*100\%$

where O_t is the absorbance of the testing samples, O_b is the absorbance of the blank groups (with no cells) and O_c is the absorbance of the control groups.

ROS scavenging activities of RuO_2@metal nanozymes. RAW264.7 cells were seeded at 1×10^4 cells per well in 12-well plates. After one day, a refreshed growth medium containing 25 μg/mL of H-RuO_2@metal nanozymes was added to cells and incubated for three additional hours. Cells were washed thrice with PBS, and then H_2O_2 (final concentration of 100 μM) was added to each well to stimulate all groups for 30 min except the negative control group. Following stimulation, the RAW 264.7 cells were incubated with DCFH-DA and Hoechst for 20 min, washed with PBS three times to remove

excess probes, and finally observed using a fluorescence-inverted microscope (Leica, Germany). The excitation wavelength was 488 nm. In addition to examination by a fluorescent microscope, H_2O_2-stimulated and DCFH-DA-incubated cells were also collected by centrifugation and analyzed by flow cytometry (cytoFLEX Flow Cytometer, USA). In principle, DCFH was transformed into the fluorescent product dichlorofluorescein in the presence of ROS, thus enabling us to gauge the quantity of intracellular ROS level.

***In vitro* anti-inflammatory effect.** After RAW264.7 cells were seeded at a density of 1×10^5 cells per well in 6-well plates for 24 h, various H-RuO_2@metal nanozymes at 10 μg/mL were added and incubated overnight. After washing the cells to remove the excess materials, 20 ng/mL LPS was introduced into the cells and incubated for 12 h. Following the manufacturer's instructions (Invitrogen), total RNA was extracted from the cells with TRIzol. Subsequently, the mRNA levels of pro-inflammatory M1 markers (IL-1β, IL-6, and TNF-α) and anti-inflammatory M2 markers (IL-10, TGF-β, and Arg-1) were determined using qRT–PCR.

***In vivo* anti-inflammatory therapies.** All animal studies were approved by the Institutional Animal Care and Use Committee (IACUC) of Nanjing University. To establish the two IBD models, male C57BL/6 mice weighing an average of 18-20 g were used. The mice were acclimatized for 7 days and randomly divided into various groups with five mice per group (n = 5). First, the CD disease model of mice was established with TNBS, and then the anti-inflammatory activities of H-RuO_2-based nanozymes were evaluated.[2] On the first day, 1 wt % TNBS solution was absorbed through the skin to presensitize the mice. Then, on day 8, mice were treated with 2.5 wt% TNBS enema, followed by the administration of nanozymes via the oral route once a day on three consecutive days (9^{th}, 10^{th}, and 11^{th} day). The mice in all groups were sacrificed after anesthetization with diethyl ether on the 12^{th} day. To establish an ulcerative colitis (UC) model, mice were fed 2% wt. DSS solution for six consecutive days, leaving one group as a control. The mice with DSS-induced UC were aseptically and orally administered H-RuO_2-based nanozymes once a day on three consecutive days (7^{th}, 8^{th}, and 9^{th}). The mice in all groups were sacrificed after anesthetization with diethyl ether on day 10. The length of the whole colon was recorded. Pathological examination and cytokine quantification with ELISA kits were performed to evaluate the therapeutic efficacy of the tested materials. Colon tissues from all groups were fixed with 10% formalin, processed, dried, embedded in paraffin, sectioned at a thickness of 4 μm, and stained with hematoxylin and eosin (H&E). The stained tissues were examined and photographed using an optical microscope. Proinflammatory cytokine evaluation (TNF-α and IL-1β) in colon homogenate was performed by homogenizing the colon tissue with a length of about 5 mm from each mouse in 1.5 mL of saline at 4 °C. The resultant homogenate was centrifuged at 2000 rpm for 20 min at 4 °C, and the supernatant was collected for evaluation. Mouse IL-1β and TNF-α ELISA Kits (Neobioscience Technology Co. Ltd., China) were used to quantify the amounts of IL-1β and TNF-α in the homogenate of colon tissues, respectively.

Biodistribution of H-RuO_2@metal nanostructures. Male C57BL/6 mice were divided randomly into different groups with 5 mice per group, receiving oral administration of H-RuO_2 and H-RuO_2@Ag nanozymes at a dosage of 5 mg/kg body weight. After different periods (*i.e.*, 12, 24, 48, and 72 h), the mice were sacrificed, and their blood, feces, heart, liver, spleen, lung, kidney, and colon were collected, weighed, boiled, and degraded with nitric acid. The content of silver in those samples was determined with an inductively coupled plasma optical emission spectrometer.

Statistical analysis. All experiments were performed in quintuplicate, and statistical analysis was performed using GraphPad Prism. One-way ANOVA was used for all other multiple-group comparisons. All the data are expressed as mean ± SD (n=5). Significant *P*-values are shown with asterisks, and *P*-

values less than 0.0001, 0.001, 0.01, and 0.05 are shown with three (****), three (***), two (**), one asterisk (*) and n.s (not significant) vs. control group, respectively.

Results and Discussion

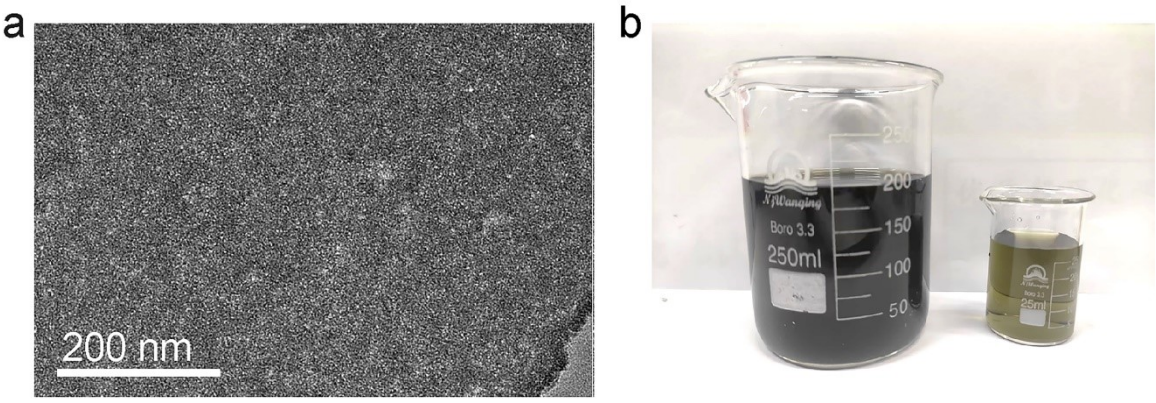

Fig. S1 (a) Low-resolution TEM image and (b) digital photo of solutions illustrating the well-dispersed, ultrasmall, and large-scale synthesis of citrate-modified H-RuO_2 NPs. A small beaker shows the concentration of the solution after 1/20 dilution with deionized water.

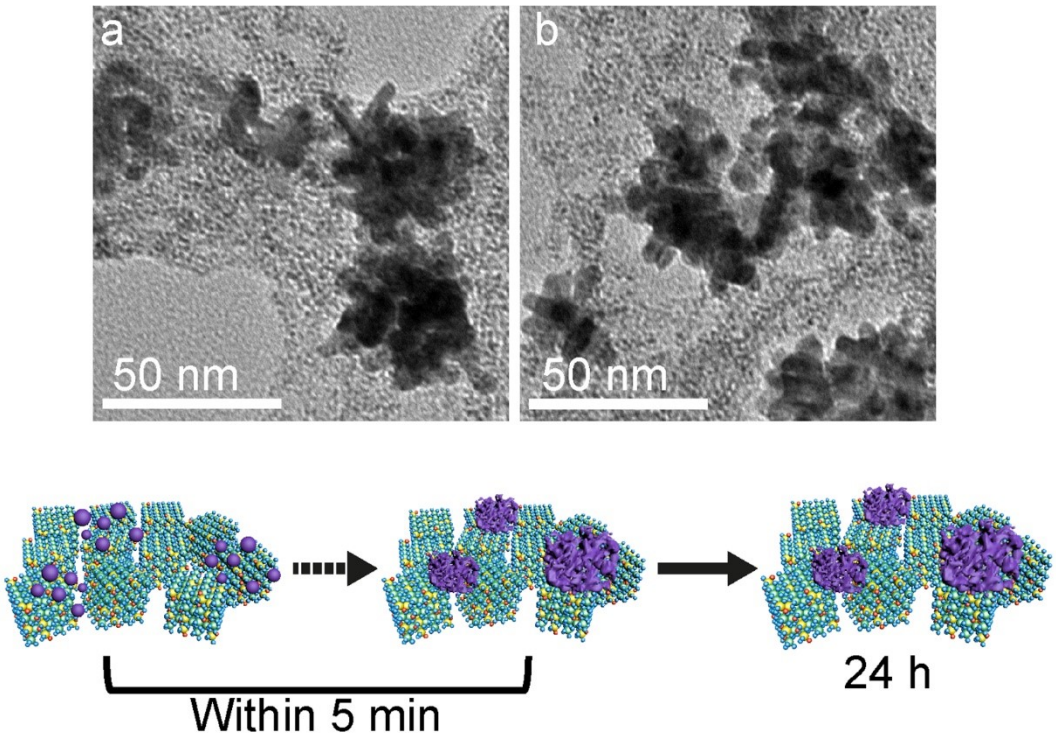

Fig. S2 Tracking the growth of self-assembled Au onto the surface of H-RuO_2 while increasing the reaction time. TEM images of H-RuO_2@ self-assembled Au analyzed after (a) 5 min and (b) after 24 h.

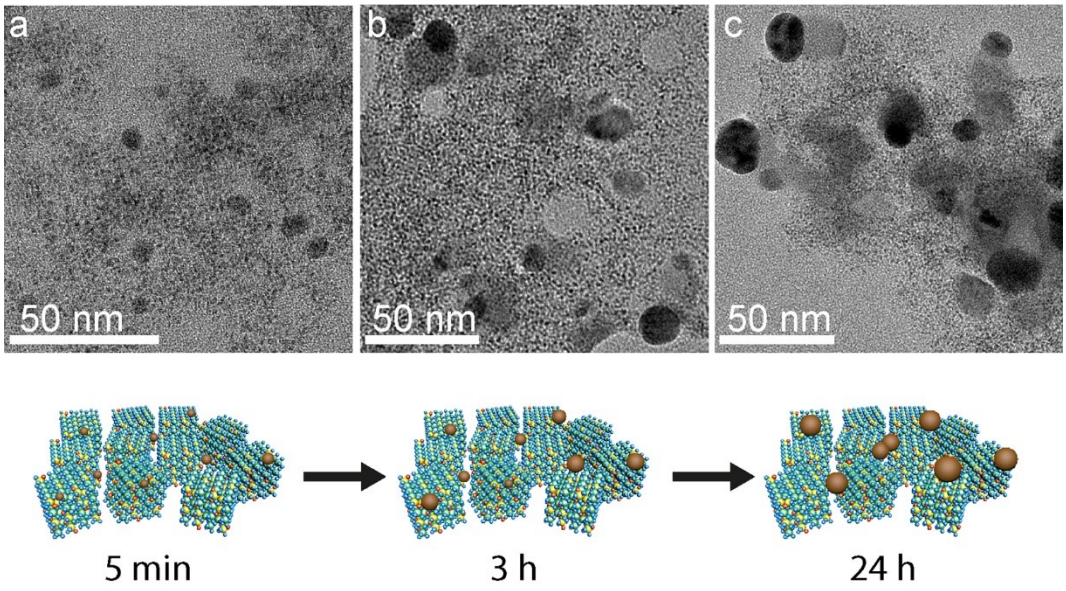

Fig. S3 Tracking the growth of Ag NPs onto the surface of H-RuO_2 while increasing the reaction time. TEM images of H-RuO_2@Ag NPs analyzed after (a) 5 min, (b) 3 h, and (c) 24 h.

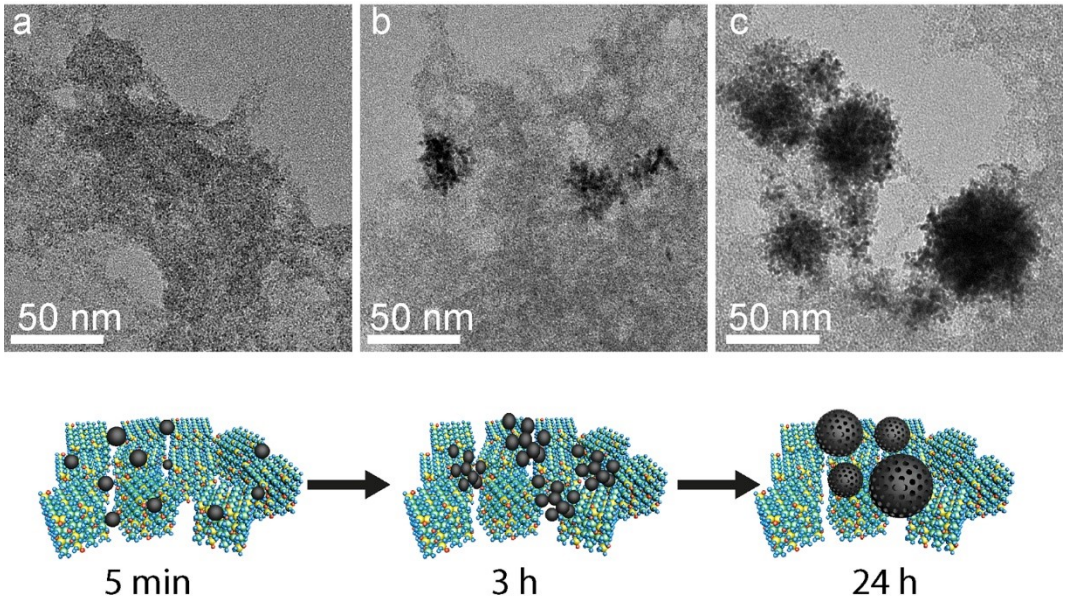

Fig. S4 Tracking the growth of Pt NPs onto the surface of H-RuO_2 while increasing the reaction time. TEM images of H-RuO_2@Pt NPs analyzed after (a) 5 min, (b) 3 h, and (c) 24 h.

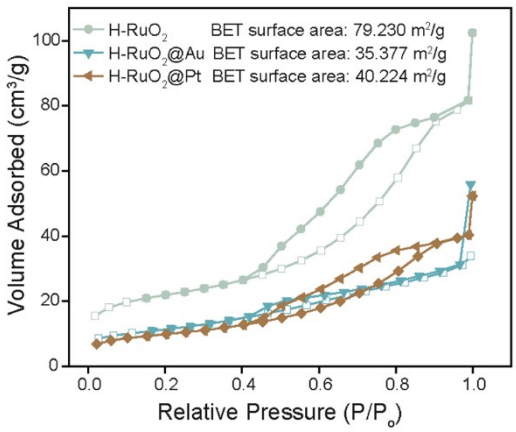

Fig. S5 Nitrogen adsorption isotherms of H-RuO_2, H-RuO_2@Au, and H-RuO_2@Pt. The BET data indicate a decrease in the surface area of H-RuO_2 after the growth of noble metals due to slight aggregation of H-RuO_2 and the loading of heavier metals such as Au and Pt.

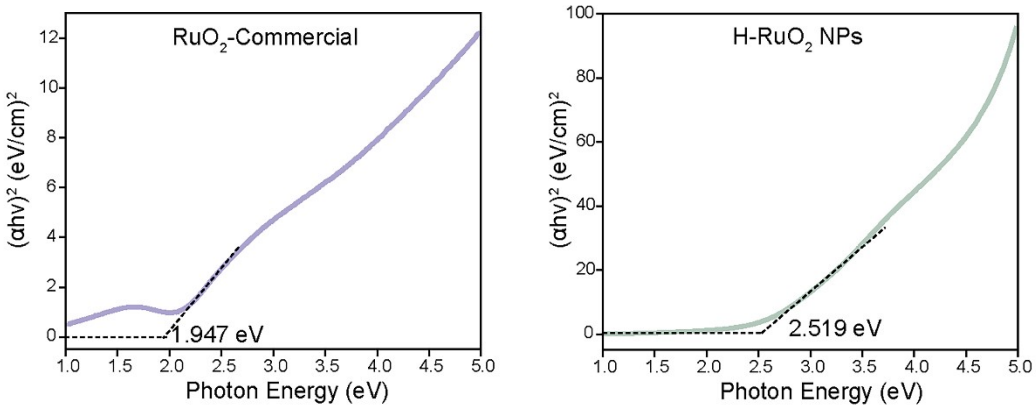

Fig. S6 Band gaps (E_g) of commercial and H-RuO_2 samples, calculated using the Tauc plot method.

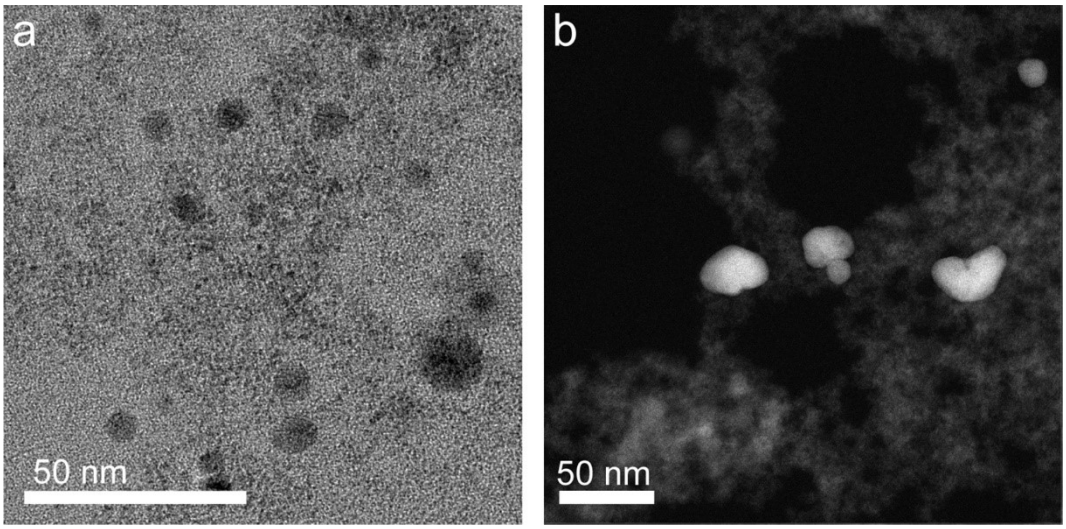

Fig. S7 Demonstrating the growth of Ag nanostructures under alkaline conditions. (a and b) TEM and HAADF-STEM images of Ag NPs grown onto the surface of H-RuO_2 NPs under alkaline conditions (pH 9.0). Upon mixing $AgNO_3$ into NH_4OH solution to achieve pH 9.0, a positively charged $[Ag(NH_3)_2]^+$ complex was *in situ* produced which reacted with the RuO_2 surface, and as a result, Ag NPs were produced.[3]

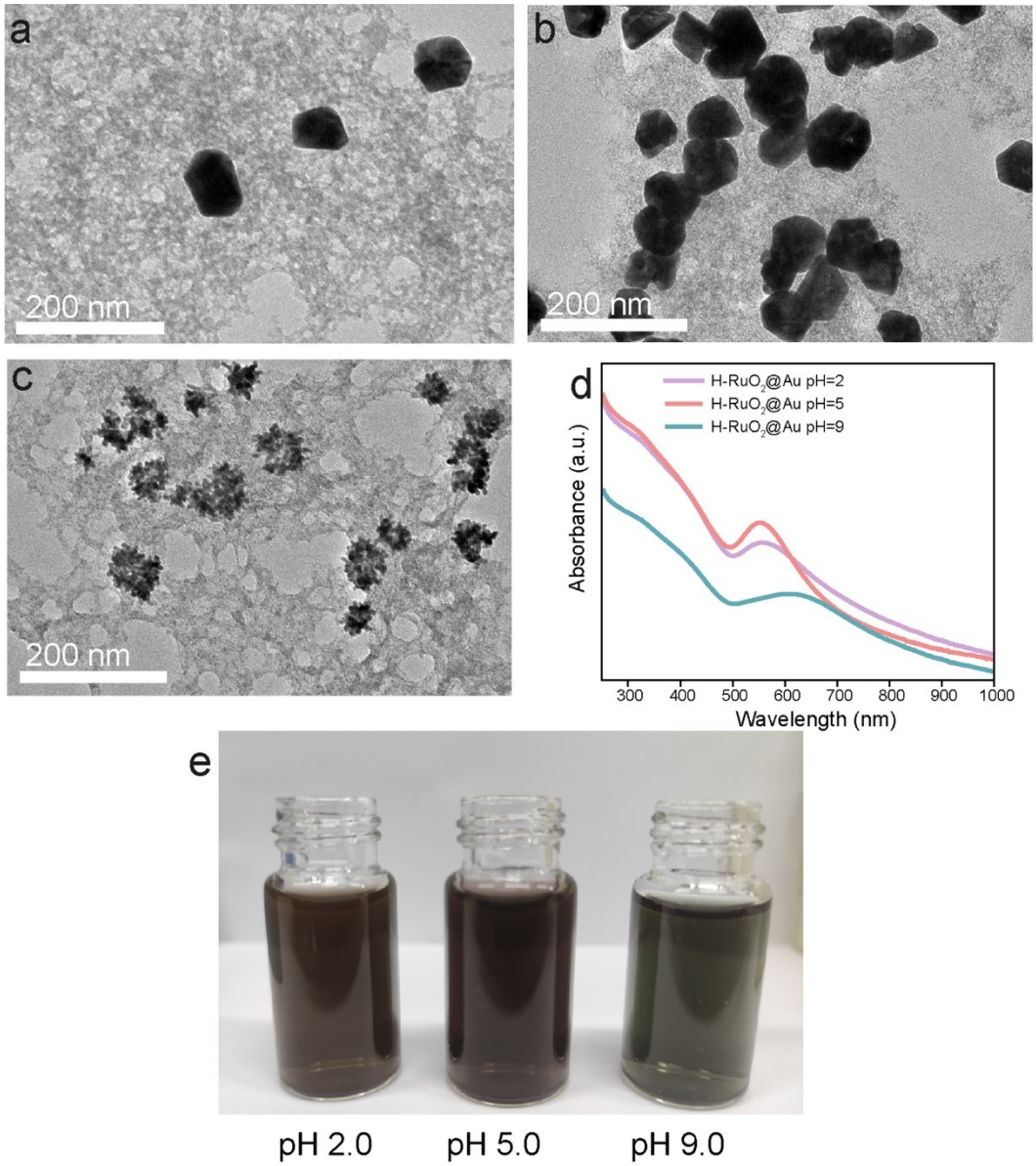

Fig. S8 Demonstrating the growth of Au nanostructures onto the surface of H-RuO_2 NPs under varying pH conditions. (a-c) TEM images of the samples prepared without pH change at pH 5.0 and pH 9.0. (d and e) Absorption spectra and the corresponding digital images of the H-RuO_2@Au samples prepared under varied pH conditions. Under alkaline conditions, $HAuCl_4$ was transformed into different negatively charged hydroxylated species, such as $AuCl_3(OH)^-$, $AuCl_2(OH)_2^-$, and $AuCl(OH)_3^-$.[4]

The samples produced at pH 2.0 and 5.0 showed strong absorption bands peaked at ~ 550 nm. In contrast, the synthesis under alkaline conditions led to a red shift of LSPR from 550 to 614 nm, accompanied by a decrease in intensity and an increase in full width at half-maximum. This red shift and broadening of the SPR peak observed in self-assembled Au were attributed to the collective electromagnetic response (delocalization of surface electrons) of self-assembled Au NPs to visible light.

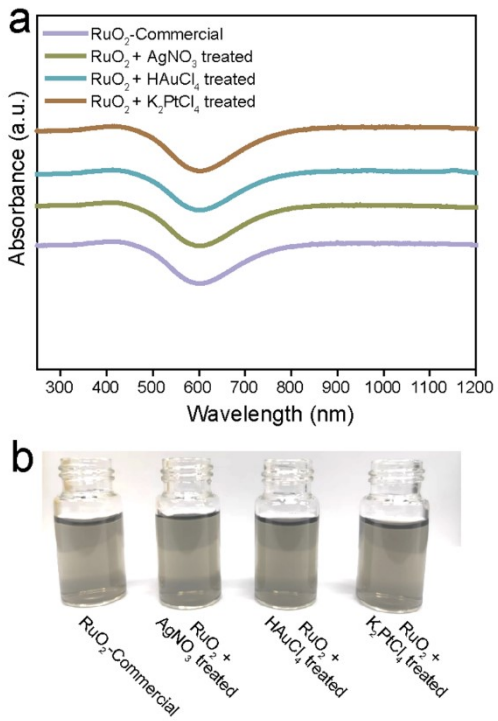

Fig. S9 Demonstrating the redox inactive nature of commercial RuO_2. (a) Absorption spectra of commercial RuO_2 before and after incubation with different metal precursors under the similar specified experimental conditions used in the case of H-RuO_2 NPs. (b) Corresponding digital photo of the samples from left to right: commercial RuO_2 and samples after treatment with $AgNO_3$, $HAuCl_4$, and K_2PtCl_4.

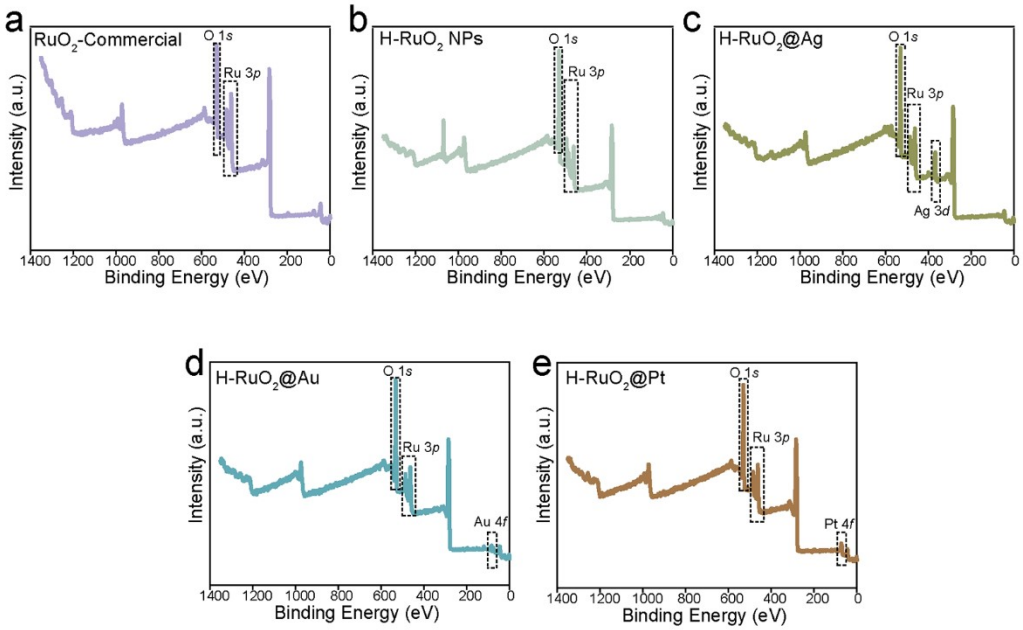

Fig. S10 XPS survey spectra. (a) Commercial RuO_2 NPs. (b) H-RuO_2 NPs. (c) H-RuO_2@Ag. (d) H-RuO_2@Au. (e) H-RuO_2@Pt nanostructures.

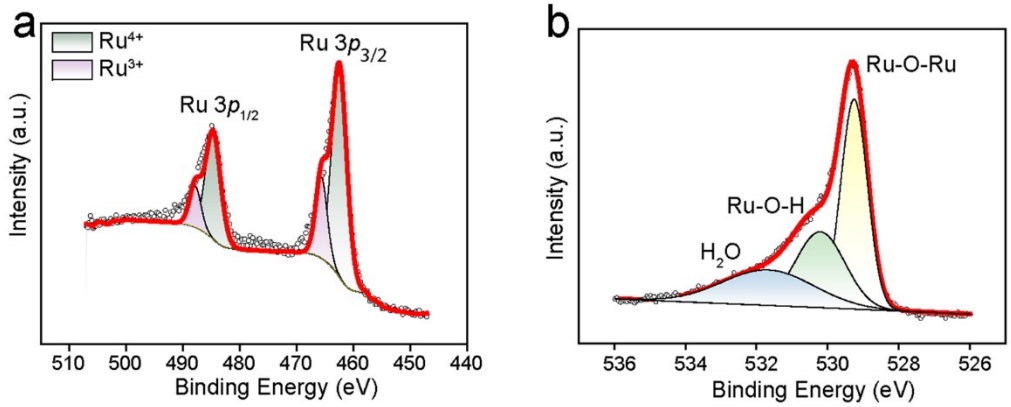

Fig. S11 High-resolution XPS spectra of commercial RuO_2. (a and b) Ru 3*p* and O 1*s*.

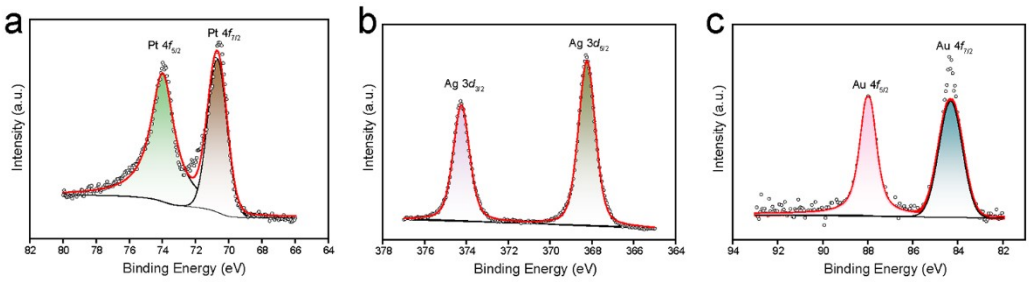

Fig. S12 High-resolution XPS spectra of H-RuO_2@metals for Pt 4*f*, Ag 3*d*, and Au 4*f*.

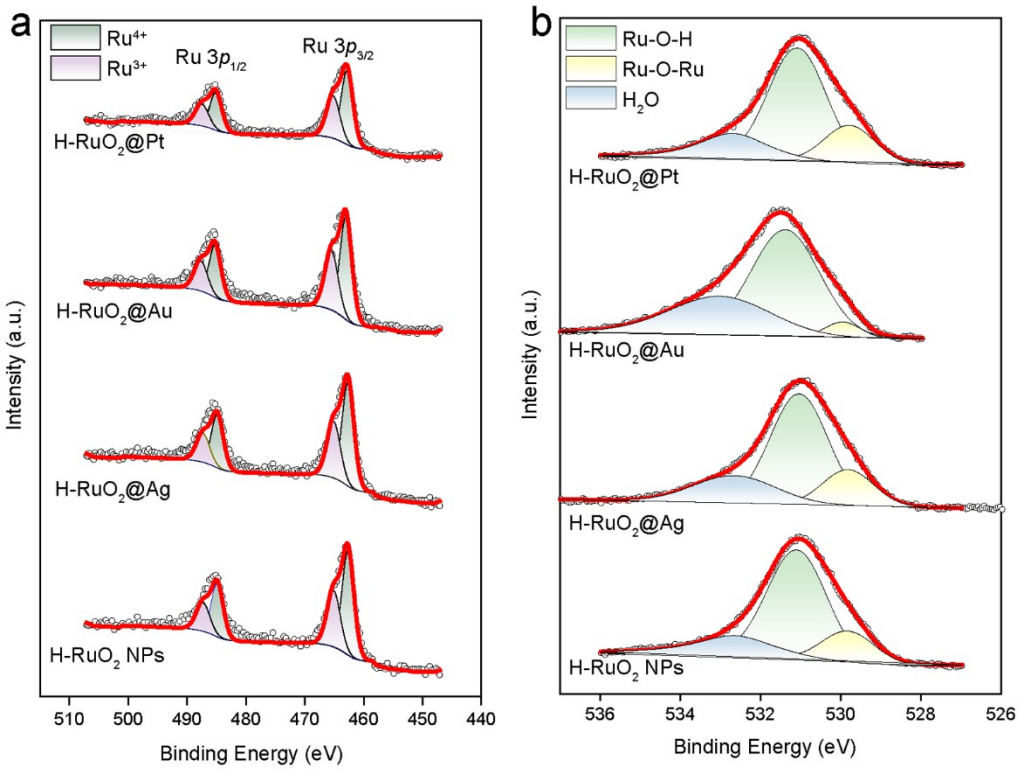

Fig. S13 XPS spectra indicate the variation in the composition of the H-RuO_2 NPs after redox reactions. (a and b) Ru 3*p* and O 1*s*.

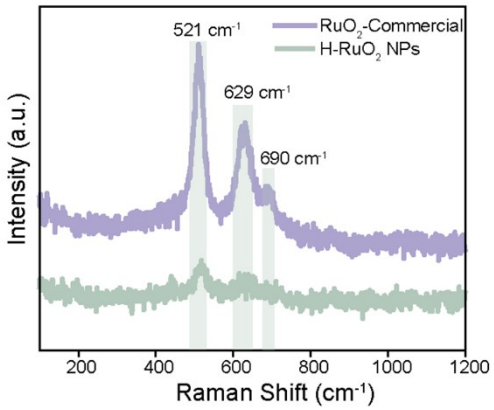

Fig. S14 Raman spectra of hydrous and commercial RuO_2 NPs.

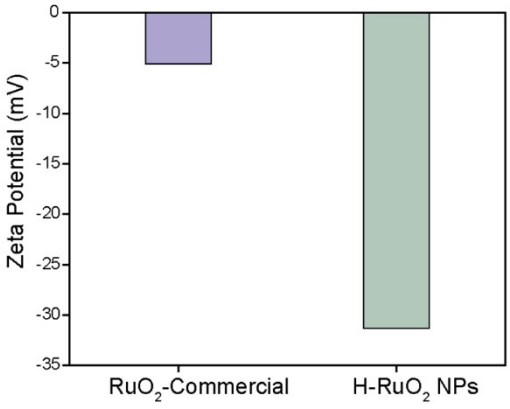

Fig. S15 Zeta potentials of hydrous and commercial RuO_2 NPs determined in deionized water at a concentration of 100 μg/mL.

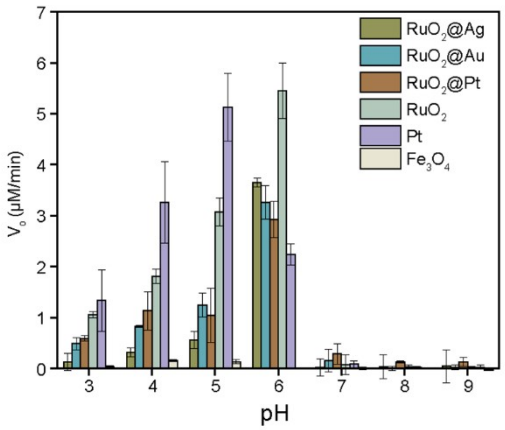

Fig. S16 Peroxidase-like activities of H-RuO_2, H-RuO_2@Ag, H-RuO_2@Au, and H-RuO_2@Pt in different pH buffers, and were also compared with well-known peroxidase nanozymes (Fe_3O_4 and Pt). The data are shown as means ± SD (n = 3).

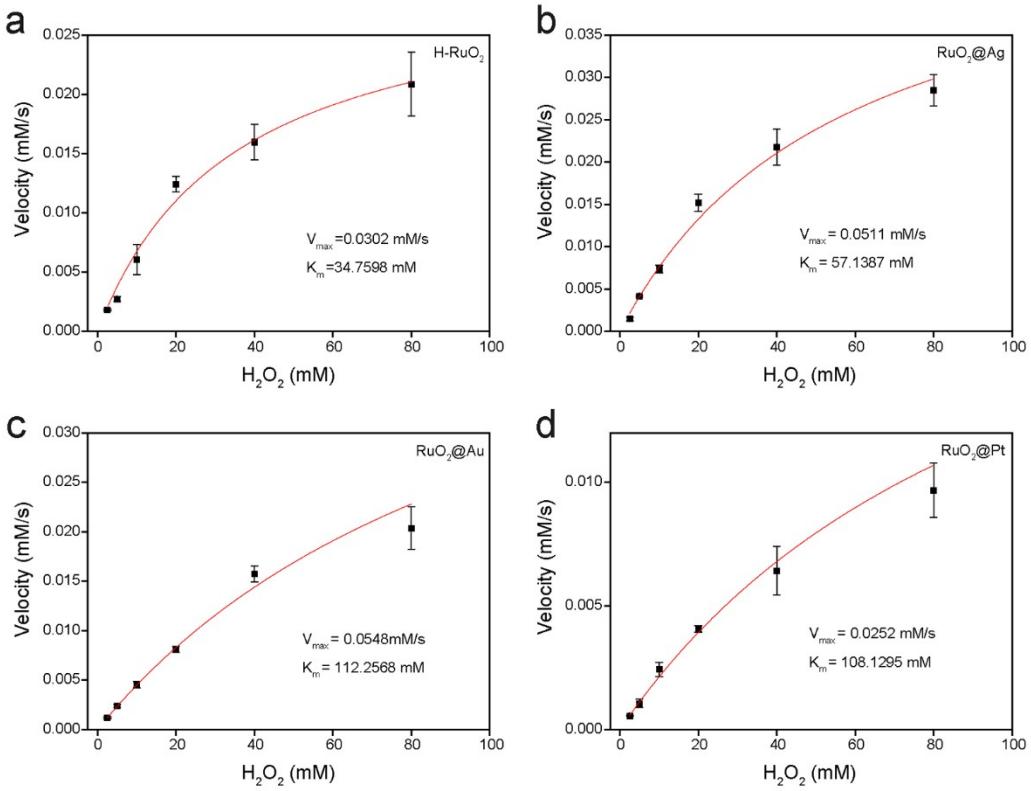

Fig. S17 Catalase-like catalytic kinetics of H-RuO_2, H-RuO_2@Ag, H-RuO_2@Au, and H-RuO_2@Pt nanostructures. The concentration of H_2O_2 was varied, and the initial reaction velocity (V) was monitored in PBS solution (pH 7.0) at 37 °C. The data are shown as means ± SD (n = 3).

K_m value shows the affinity of a substrate to an enzyme, lower K_m signifies the higher affinity of H_2O_2 towards nanozymes. The observed lower K_m values for H-RuO_2 and H-RuO_2@Ag relative to H-RuO_2@Pt and H-RuO_2@Au show a higher affinity of H_2O_2 towards silver and hydrous RuO_2 due to the presence of greater amount of oxygen vacancies in H-RuO_2 and higher oxidation susceptibility of Ag compared to Au and Pt. The differences between the V_{max} values were not so appreciable, and the values were found between 0.025-0.055mM/s, which is in agreement with the results shown in Figure 5b.

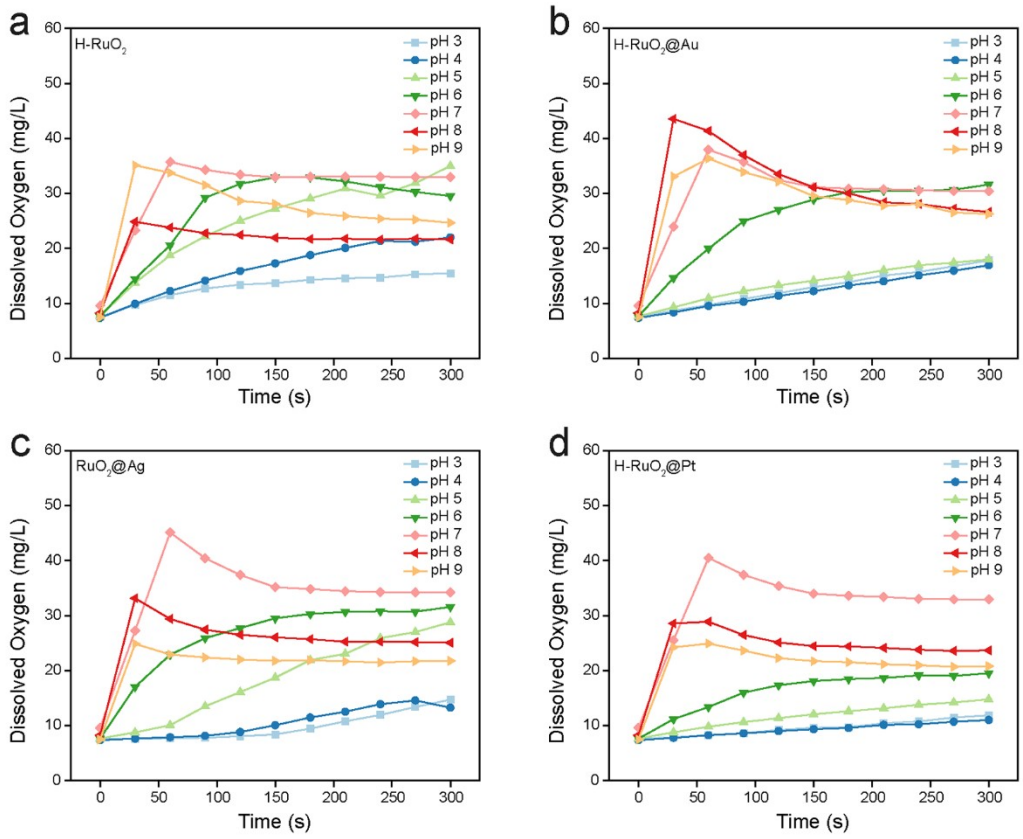

Fig. S18 Catalase-like activities of H-RuO_2, H-RuO_2@Ag, H-RuO_2@Au, and H-RuO_2@Pt in different pH buffers. The data are shown as means ± SD (n = 3).

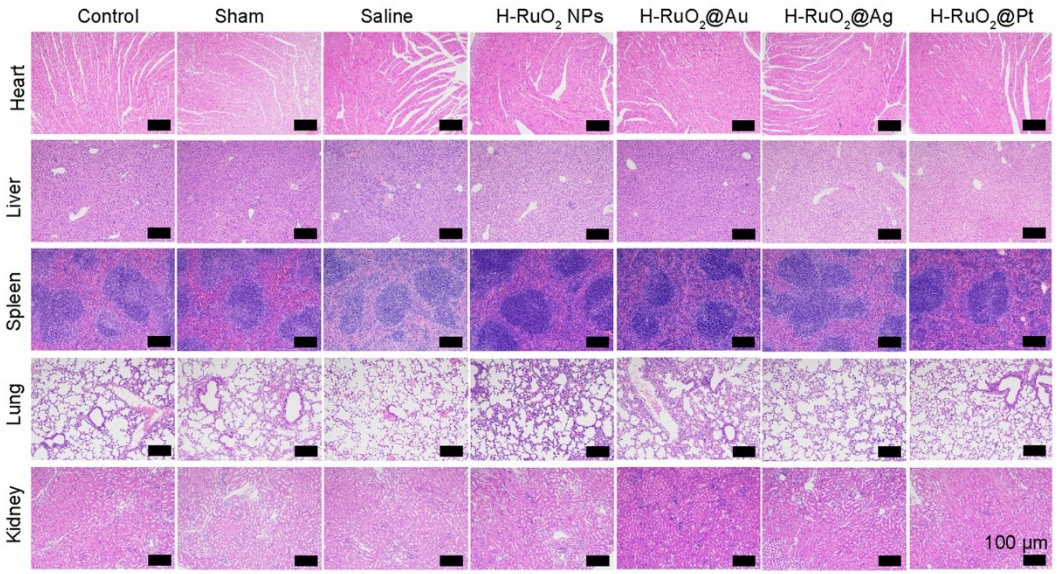

Fig. S19 Hematoxylin and eosin (H&E)-stained histological sections of different organs of mice from the indicated groups on day 12 in CD model. Scale bar 100 μm.

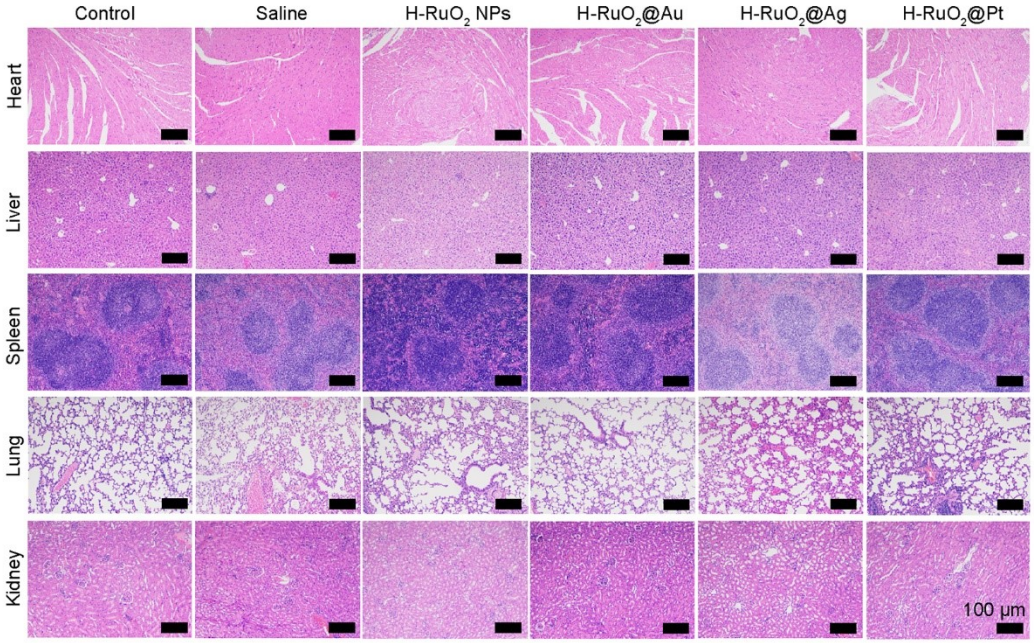

Fig. S20 Hematoxylin and eosin (H&E)-stained histological sections of different organs of mice from the indicated groups on day 10 in UC model. Scale bar 100 μm.

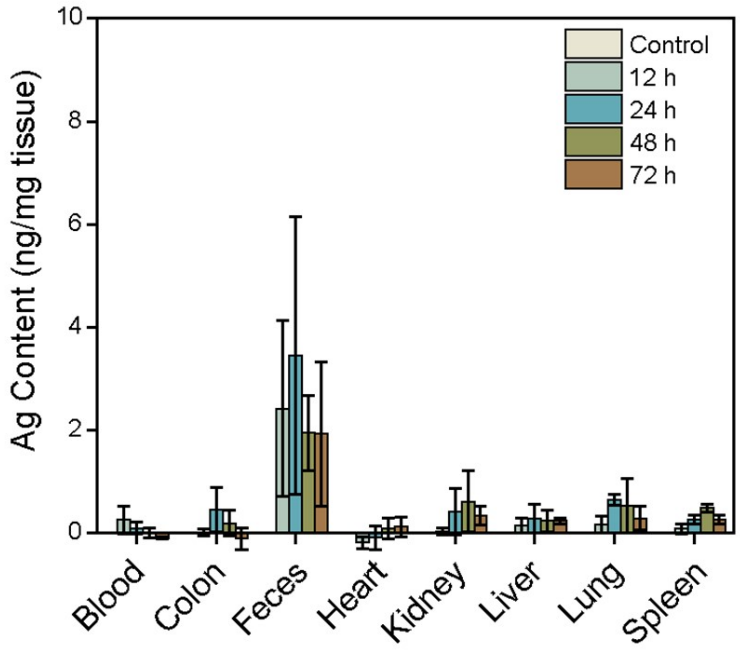

Fig. S21 Biodistribution of H-RuO_2@Ag in mouse tissues, as assessed by ICP–OES. The data are shown as means ± SD (n = 5).

To evaluate the biodistribution and biodegradation of RuO_2@metal nanostructures, we orally administered H-RuO_2 and H-RuO_2@Ag. Following different periods (12, 24, 48, and 72 h), the mice were sacrificed, and their blood, feces, heart, liver, spleen, lung, kidney, and colon were collected. The collected samples were dissolved in concentrated nitric acid at 150 °C, and the filtered solutions were analyzed using ICP–OES. However, Ru^{3+} could not be detected, most likely due to the inability of ruthenium to make a stable compound with nitric acid (ruthenium nitrate). Ruthenium only chemically exists with nitrate in the form of ruthenium(III) nitrosyl nitrate, and even for the synthesis of ruthenium(III) nitrosyl nitrate, very specified conditions are needed (by just mixing with nitric acid ruthenium(III), nitrosyl nitrate cannot be formed). In another attempt, we tried to dissolve the collected samples in aqua regia (HCl+HNO_3) but again failed to detect ruthenium due to difficulty in dissolving tissues. Finally, we indirectly determined the biodistribution and biodegradation in terms of Ag content in different organs using ICP–OES.

Table S1. Summary of measured energies (in eV) derived from UPS spectra for commercial and hydrous RuO_2 NPs.

	Work function	Valence band	Valence band maximum	Band gap	Conduction band minimum
RuO_2 NPs	4.257	0.579	-4.836	2.52	-2.317
Commercial RuO_2	4.735	1.185	-5.92	1.95	-3.973

Table S2. Primer sequences used in qPCR analysis.

Genes	Forward sequences (5'-3')	Reverse sequences (5'-3')
TNF-α	ACTCCAGGCGGTGCCTATGT	GTGAGGGTCTGGGCCATAGAA
IL-1β	TCCAGGATGAGGACATGAGCAC	GAACGTCACACACCAGCAGGTTA
IL-6	CCACTTCACAAGTCGGAGGCTTA	TGCAAGTGCATCATCGTTGTTC
IL-10	ATGCTGCCTGCTCTTACTGACTG	CCCAAGTAACCCTTA AAGTCCTGC
TGF-β	CTTCAGCCTCCACAGAGAAGAACT	TGTGTCCAGGCTCCAAATATAG
Arg-1	TGTGTCCAGGCTCCAAATATAG	AGCAGGTAGCTGAAGGTCTC
GAPDH	TGGCCTTCCGTGTTCCTAC	GAGTTGCTGTTGAAGTCGCA

References

[1] S. Zhao, Y. Li, Q. Liu, S. Li, Y. Cheng, C. Cheng, Z. Sun, Y. Du, C. J. Butch, H. Wei, *Adv. Funct. Mater.* 2020, **30**, 2004692.

[2] Y. Cheng, C. Cheng, J. Yao, Y. Yu, Y. Liu, H. Zhang, L. Miao, H. Wei, *Adv. Ther.* 2021, **4**, 2100081.

[3] L. Wang, L. Yan, L. Ye, J. Chen, Y. Li, Q. Zhang, C. Jing, *JACS Au* 2022, **2**, 1435-1442.

[4] T. Kayama, K. Yamazaki, H. Shinjoh, *J. Am. Chem. Soc.* 2010, **132**, 13154-13155.